JOURNAL OF APPLIED CRYSTALLOGRAPHY

ISSN 1600-5767

Received 9 January 2019
Accepted 12 June 2019

Edited by S. Boutet, SLAC National Accelerator Laboratory, Menlo Park, USA

Keywords: aerosols; droplet size; gas dynamic virtual nozzles (GDVNs); environmental scanning electron microscopy; coherent X-ray diffractive imaging (CXDI); single particles; sample delivery; structural biology; nanoscience.

Nanometre-sized droplets from a gas dynamic virtual nozzle

Kerstin Mühlig,[a] Alfonso M Gañán-Calvo,[b] Jakob Andreasson,[a,c,d] Daniel S. D. Larsson,[a] Janos Hajdu[a,c]* and Martin Svenda[a,e]*

[a]Laboratory of Molecular Biophysics, Department of Cell and Molecular Biology, Uppsala University, Husargatan 3 (Box 596), Uppsala, SE-751 24, Sweden, [b]Departmento de Ingeniería Aerospacial y Mecánica de Fluidos, ETSI, Universidad de Sevilla, Sevilla, ES-410 92, Spain, [c]Institute of Physics, ELI Beamlines, Academy of Sciences of Czech Republic, Prague, CZ-182 21, Czech Republic, [d]Condensed Matter Physics, Department of Physics, Chalmers University of Technology, Gothenburg, SE-412 58, Sweden, and [e]Biomedical and X-ray Physics, Department of Applied Physics, KTH/ Royal Institute of Technology, KTH-AlbaNova, Stockholm, SE-106 91, Sweden. *Correspondence e-mail: janos.hajdu@icm.uu.se, martin.svenda@biox.kth.se

This paper reports on improved techniques to create and characterize nanometre-sized droplets from dilute aqueous solutions by using a gas dynamic virtual nozzle (GDVN). It describes a method to measure the size distribution of uncharged droplets, using an environmental scanning electron microscope, and provides theoretical models for the droplet sizes created. The results show that droplet sizes can be tuned by adjusting the gas and liquid flow rates in the GDVN, and at the lowest liquid flow rates, the size of the water droplets peaks at about 120 nm. This droplet size is similar to droplet sizes produced by electrospray ionization but requires neither electrolytes nor charging of the solution. The results presented here identify a new operational regime for GDVNs and show that predictable droplet sizes, comparable to those obtained by electrospray ionization, can be produced by purely mechanical means in GDVNs.

1. Introduction

The list of applications using nanometre-sized droplets is extensive and rapidly growing. It ranges from numerous fields in physics, chemistry and biology to industrial applications. These include studies in cluster physics, mass- and ion-mobility spectrometry (Uetrecht *et al.*, 2010; Shang *et al.*, 2017), aerosolized pharmaceuticals and cosmetics (Patel & Vavia, 2007; Wu *et al.*, 2013), and experiments where container-free sample handling is needed to study isolated particles, macromolecules (Seibert *et al.*, 2011; van der Schot *et al.*, 2015) or nano-crystals (Awel *et al.*, 2018). The motivation for the present study was our need to tune the droplet size for container-free sample handling for lens-less imaging experiments of single macromolecules and larger bio-particles with X-ray lasers or pulsed electron sources. In these studies, droplet sizes have to be tailored to match sample sizes. Of particular importance is the fact that the smaller the volume of a droplet, the lower the quantity of non-volatile contaminants entrapped in the droplet, and thus macromolecules emerge in a cleaner form from smaller drops than from larger ones (Daurer *et al.*, 2017). Small droplets also reduce the probability of trapping more than one macromolecule in a single droplet and thus reduce the risk of unwanted cluster formation as droplets shrink during evaporation.

Here we show that modern variants of the gas dynamic virtual nozzle (GDVN) (DePonte *et al.*, 2008; Gañán-Calvo,

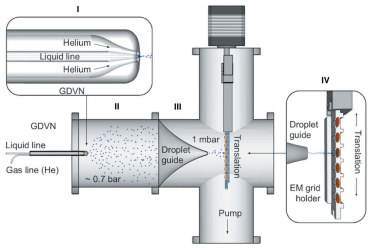

1998; Gañán-Calvo *et al.*, 2010) offer a means to create extremely small droplets from an aqueous sucrose solution that are similar in size to droplets produced by electrospray ionization (ESI), but requiring neither an electrolytic solvent nor application of a high-voltage potential across the solution. In contrast, in GDVNs a narrow jet is produced by a co-flowing gas, which constricts the sample jet as a solid aperture would, before it eventually disintegrates into a stream of small droplets. The physical opening of the nozzle is not tapered, thus reducing the risk of clogging. The results show that GDVNs can be tuned to generate droplets in a broad size range extending below 120 nm in diameter.

In ESI droplet generation, a differential mobility analyser is employed for characterization of particle size distribution, but such instruments require controlled particle charging and are sensitive to extra gas flow as applied in GDVNs. The development of the method to measure the size distribution of droplets described here, using an environmental scanning electron microscope (ESEM), allows particle characterization without sample charging. It opens possibilities for the systematic development of GDVNs to introduce very small objects into the gas phase in a clean form, free from additives, electrolytes or debris, and without the need for electrically charged particles.

2. Methods

2.1. Investigation of evaporation of aqueous sucrose droplets in vacuum

The observation setup for the droplet evaporation is shown in Fig. 1. A solid deposition substrate was installed at an oblique angle to the electron beam (electron cone) inside a FEI QUANTA 650 field emission gun (FEG) ESEM. A Kleindiek micro-injector (model MIS-EM) was mounted on a micromanipulator (model MM3A-EM) to deposit droplets onto the target. The pressure inside the ESEM chamber was 1 mbar (1 bar = 10^5 Pa). The micro-injector was connected to a valve-gated nanoflow pump outside the chamber through a side port via a 50 µm-inner-diameter capillary. Droplet deposition and evaporation of the droplets were observed in real time either with a large-field detector or with the gaseous secondary electron detector of the FEI QUANTA 650 FEG.

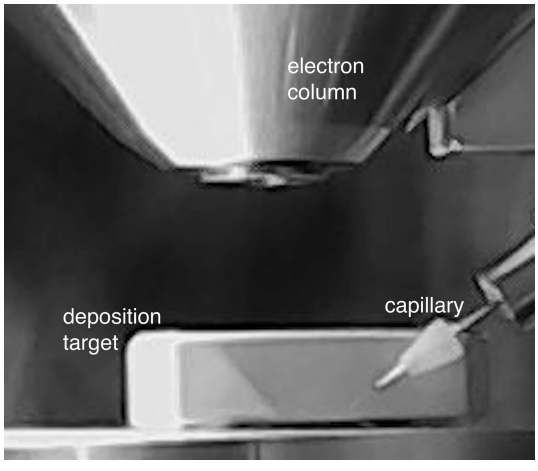

Figure 1
Experimental setup to observe droplet deposition in real time inside an ESEM. A solid deposition substrate was mounted at an oblique angle to the electron beam (electron cone) inside the ESEM. A micro-injector was mounted on a micromanipulator to deposit droplets onto the target.

2.2. Measuring droplet sizes generated by a GDVN at different liquid flow rates

The experimental setup for droplet deposition onto electron microscopy (EM) grids is shown in Fig. 2. It consists of the GDVN housing (*a*II), where the GDVN is inserted, operating in a helium atmosphere at near atmospheric pressure

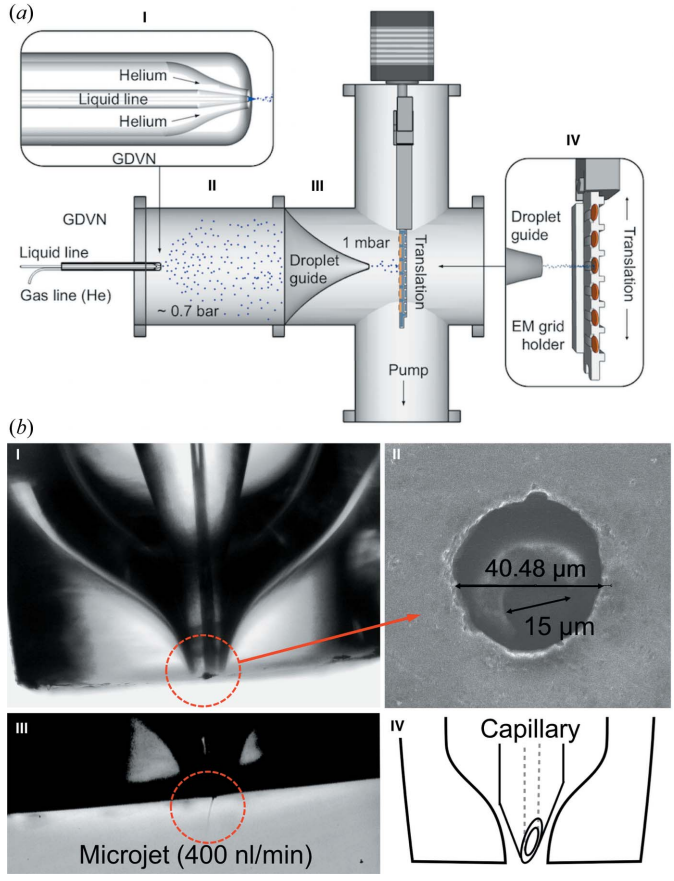

Figure 2
(*a*) Experimental setup for droplet depositions onto EM grids. (*a*I) The GDVN produces an aerosol from a 1% sucrose solution. (*a*II) The GDVN housing (first chamber), operating at near atmospheric pressure. (*a*III) The droplet deposition chamber at 1 mbar. (*a*IV) Set of EM grids that can be moved up and down to be exposed to the droplet stream for measuring imprints. (*b*) A schematic and images of the tip of the GDVN used here. Panel (*b*I) shows a lateral view of the geometry with the convergent nozzle region. Panels (*b*II) and (*b*IV) depict the partially bevelled tip of the liquid capillary, whose advanced edge is approximately centred on the discharge section (top view and longitudinal section, respectively). Panel (*b*III) demonstrates the ejection of a micro-jet visible in an optical microscope at a liquid flow rate of 400 nl min^{-1}. At flow rates lower than 350 nl min^{-1}, no jet was visible but droplets were still formed as judged by the deposition on the EM grids.

(0.7 bar), the droplet deposition chamber at 1 mbar (*a*III), and a set of EM grids mounted on a translation stage (*a*IV). The GDVN produces aerosols from a 1%(*v*/*v*) sucrose solution by coaxial flow of helium gas to create a narrow liquid jet prior to its breakup. We used a high-speed camera (model Fastcam SA-4, Photron) to monitor the operation of the GDVN during the experiments. Liquid flow rates were measured with a Sensirion flow meter (model SLG1430). In the GDVN, the pressures of the helium sheath gas were 24–41 bar upstream of the supply line. The estimated ideal helium mass flows through a GDVN with a 40.5 µm-wide opening lie between 0.173 and 0.294 g min^{-1}. The actual flow is primarily limited by contraction of the stream and linked to the ideal mass flows through the discharge coefficient of the nozzle. The discharge coefficients vary, in general, from 0.5 to 0.7. Large nozzles usually have higher efficiencies than small nozzles. So, we expect discharge coefficients of about 0.5–0.6 at the GDVN and slightly higher at about 0.6–0.7 at the funnel to the next chamber. This is in balance with the resulting pressures of 0.4–0.7 bar in the first chamber at helium pressures of 24–41 bar upstream of the supply line.

The pressure driving the sample flow was between 18 and 35 bar. These values were individually set to obtain optimal aerosol formation conditions and constant sample flow rates at 200, 300, 350 or 400 nl min^{-1}. All measurements were performed with one selected GDVN.

The GDVN housing (first chamber) is connected to the droplet deposition chamber via a nozzle with a 0.3 mm exit hole. Droplets are funnelled through this orifice into the droplet deposition chamber, driven by the difference in pressure, 0.7 bar in the first chamber and 1 mbar in the droplet deposition chamber. The helium intake from the GDVN keeps the first chamber at about 0.7 bar during operation. Calculation of the gas discharge through the 0.3 mm aperture with a 0.699 bar pressure drop yields 0.273 g min^{-1} of helium. Knowledge of this mass flow rate is essential to calculate the partial water vapour pressure at the first chamber. This is approximately equal to the ratio of mass flow rates of water through the GDVN and of helium through the first chamber, assuming that the maximum practicable amount of the water in the droplets evaporates (which is subsequently demonstrated). A set of EM grids from Ted Pella (Formvar/carbon-coated copper grids, mesh 400) were placed on a motorized translation stage at a distance of 10 mm from the tip of the droplet guide [Fig. 2(*a*IV)]. The stage can be moved up and down at a speed of about 10 mm s^{-1} to allow exposure of all grids to the droplet stream for measuring imprints. The EM grids were imaged in the FEI QUANTA 650 FEG at high vacuum (about 10^{-6} mbar). Micrographs were taken using the retractable STEM III detector of the microscope at 20–30 kV accelerating voltage. As a control, several EM grids that were not exposed were imaged. The size distribution of the droplet deposits was evaluated using the software package *ImageJ* (Abramoff *et al.*, 2004; Schneider *et al.*, 2012).

Thereafter an extra set of experiments were performed in support of the previous approach. The dried sucrose deposits on the EM grids were directly measured with an atomic force microscope (AFM). In preparation, 'sprayed on' EM grids were glued onto magnetic AFM specimen discs. Numerous deposits were scanned with a micro cantilever in AC Air topography mode using an AFM (model Cypher, Asylum Research). The data were post-processed with the provided instrument software (Asylum Research) to extract footprint diameter and volume.

3. Results and discussion

3.1. Investigating how droplets of an aqueous sucrose solution evaporate in low vacuum

We performed experiments to investigate the evaporation of dilute sucrose solutions under a variety of conditions and then used the acquired knowledge in the next set of experiments to investigate the distribution of droplet sizes.

Figs. 1 and 3 show the evaporation of large single droplets monitored in real time inside an ESEM at a pressure of 1 mbar. We deposited water droplets and droplets of aqueous sucrose solutions [0.1–10%(*v*/*v*)] of several micrometres in diameter with the help of a micro-injector onto a solid surface inside the ESEM (Fig. 1) and monitored their evaporation in real time. The results (Fig. 3) show that a water droplet with a footprint of 200 µm completely evaporates within about 2 s, but a droplet of a 1% sugar solution leaves behind a glassy residue that does not change further after about 12 s.

Moreover, we inserted a GDVN inside the ESEM and followed the direct deposition of 20 µm sucrose droplets [∼1000 times smaller volume than the water droplet in Fig. 3(*a*)] with the GDVN placed less than 0.5 mm away from the surface [Fig. 3(*c*)]. Both studies established that the footprints of the droplets did not change measurably during evaporation of water in the vacuum chamber of the ESEM [Figs. 3(*b*) and 3(*c*)] and that the sucrose domes left behind after evaporation maintained their shape and dimensions over several hours *in vacuo*, suggesting that sublimation of solid sucrose was negligible. Note also that the footprint of a droplet with a fixed volume depends on the impact velocity.

3.2. Measuring droplet sizes generated by a GDVN at different liquid flow rates

Next we used a GDVN to generate very fine droplets from a 1% sucrose solution and measured the diameter of these sucrose deposits on an EM grid. The purpose is, using the acquired knowledge from the previous experiments on droplet evaporation behaviour, to be able to back calculate the original droplet size of the sucrose deposits. The experimental setup is shown in Fig. 2(*a*).

Droplets start evaporating as soon as they leave the GDVN. The concentration of sucrose increases along the flight path. Equation (1) (Holyst *et al.*, 2013) estimates the vapour pressure at the droplet surface to calculate the evaporation rate of freely suspended single droplets, as is the situation in the first chamber (GDVN housing) shown in Fig. 2(*a*II). From equation (1), we estimate the 'impact concentration' of the sugar droplets as follows. That pressure is given by

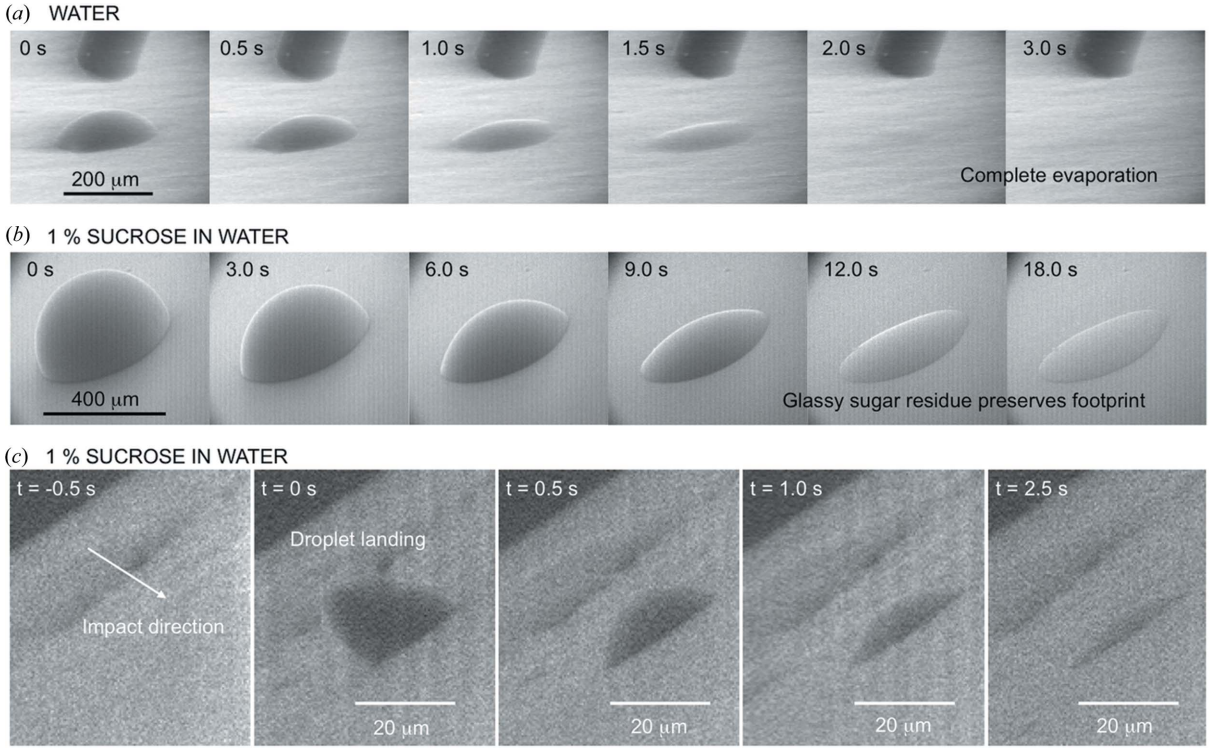

Figure 3
Evaporation of a water droplet (*a*) and a droplet of a 1% sucrose solution (*b*) generated by a micro-injector at 1 mbar pressure as monitored in an ESEM. The results show that evaporation of droplets with 20–400 μm diameter takes several seconds. Evaporation of a 1% sucrose droplet leaves behind a vitreous sucrose residue whose diameter is similar to the diameter of the original droplet. (*c*) A typical impact of a 1% sucrose droplet generated by a GDVN mounted inside the ESEM. The distance of the droplet source from the surface was about 0.5 mm. The elongated appearance of the impacting droplet in the second image of series (*c*) is due to small delays in scanning with the electron beam in the vertical direction during the movement of the droplet. The footprint of sucrose droplets did not change during drying.

$$p_{\rm a}(T_{\rm L}) = p_{\rm sat}(T_{\rm L}) \exp\left[\frac{M}{RT_{\rm L}\rho_{\rm L}}\frac{2\gamma}{a} - \frac{n_{\rm s}}{(a/a_0)^3 - n_{\rm s}}\right], \quad (1)$$

where $p_{\rm a}$ and $p_{\rm sat}$ are the partial vapour pressure at the surface and the equilibrium saturation vapour pressure at a given temperature $T_{\rm L}$ of the droplet surface in the liquid phase. Given the smallness of the droplets, $T_{\rm L}$ is nearly equal to the ambient temperature (Holyst *et al.*, 2013). M, R and $\rho_{\rm L}$ are the molecular mass of the liquid/vapour, the universal gas constant and the density of the liquid, γ is the surface tension of the liquid, $n_{\rm s}$ is a constant approximately equal to the initial mass fraction of impurities, and a_0 and a are the initial and final droplet radius. While $p_{\rm a}$ is larger than the partial pressure of vapour in the chamber, water vapour rapidly diffuses away from the droplet surface and the droplet evaporates continuously. Given the small size of the droplets (micrometre size), this process is very rapid (of the order of milliseconds; Holyst *et al.*, 2013). Assuming that no further evaporation takes place when $p_{\rm a}$ reaches the value of the vapour pressure in the chamber, equation (1) yields the droplet size corresponding to each water flow rate through the GDVN. The gas temperature is assumed to be equal to that in the laboratory. Given the small size of the droplets, their temperature is that of the gas (*i.e.* $T_{\rm L}$ = 293 K), which yields a water saturation pressure $p_{\rm sat}(T_{\rm L})$ = 0.023 bar. The ratio of water and total helium mass flow rates is assumed to be equal to the partial water vapour pressure in the first chamber. To show this, we should demonstrate that the maximum practicable amount of the water in the droplets evaporates. First, from the relationship between mass and volume concentrations one initially has $(a_{\rm s}/a_0)^3 = c_{\rm initial} = n_{\rm s}[(\rho_{\rm s}/\rho_L)(1-n_{\rm s}) + n_{\rm s}]^{-1} \cong n_{\rm s}\rho_{\rm L}/\rho_{\rm s}$, for $n_{\rm s} \ll 1$, where $a_{\rm s}$ is the radius of the solid sucrose ball that an initial droplet with radius a_0 would leave after complete evaporation. For $n_{\rm s} = 0.01$ and the density of sucrose $\rho_{\rm s} = 1.59\rho_{\rm L}$, we have $(a_{\rm s}/a_0)^3 = 0.0063$ in all cases. Next, from equation (1) we have

$$\frac{M}{RT_{\rm L}\rho_{\rm L}}\frac{2\gamma}{a} - \frac{n_{\rm s}}{(a/a_0)^3 - n_{\rm s}} = \ln\left[p_{\rm a}(T_{\rm L})/p_{\rm sat}(T_{\rm L})\right], \quad (2)$$

where $[2M\gamma/(RT_{\rm L}\rho_{\rm L})] = 1.07$ nm, a very small length compared with the vast majority of droplets. Thus, one has $M/(RT_{\rm L}\rho_{\rm L})(2\gamma/a) \ll n_{\rm s}/[(a/a_0)^3 - n_{\rm s}]$. This simplification together with the expression for $c_{\rm initial}$ allows us to calculate the droplet volume reduction by evaporation:

$$\left(\frac{a_{\rm s}}{a}\right)^3 = \frac{c_{\rm initial}}{(a/a_0)^3} = \frac{\rho_{\rm L}}{\rho_{\rm s}} \Big/ \left\{1/\ln\left[\frac{p_{\rm sat}(T_{\rm L})}{p_{\rm a}(T_{\rm L})}\right] + 1\right\}. \quad (3)$$

Note that the initial concentration of sucrose is gone. This expression yields approximately 50%(*v*/*v*) sucrose concentration for the water flow rates used in our experiments (with errors below 5% for liquid flow rates from 200 to 400 nl min^{-1},

and pressures of the first chamber between 0.4 and 0.7 bar). Thus, some water is trapped inside the free-flying droplets under the conditions inside the first chamber prior to the discharge funnel, but at least 98.5% of the water in the droplets is evaporated in the first chamber (*i.e.* only a small fraction equal to $n_s\{1/\ln[p_{sat}(T_L)/p_a(T_L)]+1\}$ of the initial water volume remains in the droplet). The evaporation within the second chamber can be neglected, because of the small distance between the exit of the funnel and the grids and the increased velocity of the particles after the funnel. Particles travel shorter flying times than 20 µs. Furthermore, the high sucrose concentration reduces the evaporation rate greatly.

Finally, to calculate the initial droplet size $d_{initial}$ we exploit our observation that the footprint of deposited sucrose droplets $d_{deposit}$ does not change further during evaporation [Figs. 3(*b*) and 3(*c*)] on the surface. Thus we can estimate the volume at impact from the size of the footprint of the sucrose residue under the assumption that the sucrose balls adopt a hemispherical shape. Then we use the initial concentration $c_{initial}$ and the calculated sucrose concentration from equation (1) at the time of impact c_{impact} to infer the diameter of the droplets leaving the GDVN. By conservation of mass (of the non-volatile sucrose),

$$d_{initial} = \left(\frac{1}{2}\frac{c_{impact}}{c_{initial}}\right)^{1/3} d_{deposit}. \quad (4)$$

Close-up images of the GDVN used in the experiments are given in Fig. 2(*b*). Three typical operation modes of a GDVN have been identified by DePonte *et al.* (2008): dripping, spurting and jetting modes. Dripping appears at low gas and liquid pressures and produces large droplets. Periodic spurting occurs at high gas pressures and low liquid pressures, while jetting creates a stable and narrow liquid jet that breaks up into small droplets to create some of the finest aerosols. We used a high-speed camera to monitor the operation of GDVNs during the experiments.

The pressure of the helium sheath gas was set to a value between 24 and 41 bar, and the flow rate in the liquid line was set to 200, 300, 350 or 400 nl min^{-1}. The overall pressure in the first chamber [Fig. 2(*a*II)], the housing of the GDVN, was ∼0.7 bar. The droplets were transported from this chamber downstream by the helium gas and then accelerated through a conical nozzle (droplet guide) of 0.3 mm exit diameter into a second chamber [Fig. 2(*a*III)], which was pumped to 1 mbar pressure. EM grids, coated with carbon, were placed on a motorized translation stage at a distance of 10 mm from the tip of the droplet guide.

By adjusting pressures in the liquid and sheath gas lines, the GDVN can be taken through an array of operating modes where aerosols of different properties are formed. It should be noted that the characteristics of GDVNs depend strongly on the micro-fabrication details and the operating parameters, and each GDVN requires individual optimization of the operating parameters to meet specific demands. In the present study, we investigated the droplet size, radial spread and size homogeneity of the aerosols produced by one selected nozzle, shown in Fig. 2(*b*). The GDVN was operated under conditions similar to those for which successful single-particle imaging experiments have been performed at the LCLS X-ray free-electron laser but at much lower liquid flow rates (van der Schot *et al.*, 2015; Seibert *et al.*, 2011; Ekeberg *et al.*, 2015; Hantke *et al.*, 2014). The high-density aerosol leads to rapid deposition of droplets on the EM grid. To reduce the problem of multiple droplets being deposited on top of each other we implemented a motorized translation stage to streak the EM grids across the aerosol stream at a speed of about 10 mm s^{-1} [Fig. 2(*a*IV)]. Following droplet deposition, the EM grids were transferred into the ESEM, and the dry sucrose deposits were classified in size and radial distribution in high-vacuum mode (about 10^{-6} mbar) at 20–30 kV accelerating voltage. Figs. 4 and 5 show typical EM images of deposited sucrose residues.

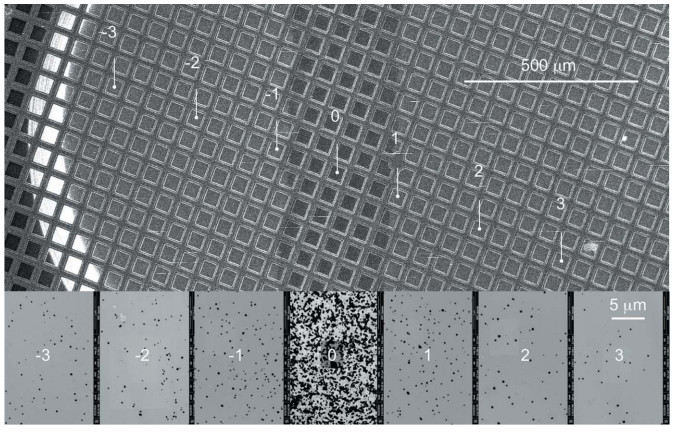

Figure 4
ESEM image of an EM grid with sugar droplets deposited on the grid during translation at 10 mm s^{-1} in front of the aerosol stream. The bottom row shows a series of high-resolution EM images taken at the locations marked above. Zero marks the centre of the track behind the focused aerosol beam as the grid was translated. The width of the central line is approximately 250 µm, with a large number of small droplets deposited on the grid in such numbers that their impact points overlap to form irregular aggregates.

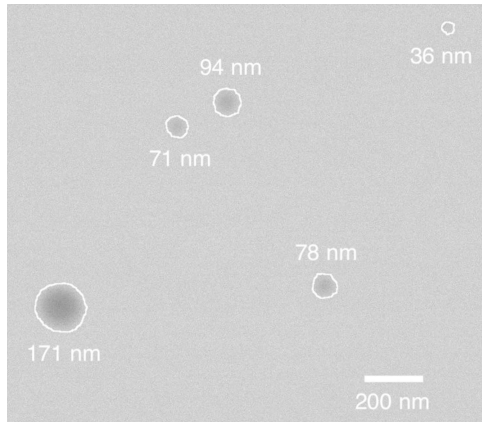

Figure 5
A digitally zoomed in close-up of an EM image of deposited sucrose residues on an electron microscopy grid. Initial sucrose droplets were created by a GDVN with a liquid flow rate set to 200 nl min^{-1}.

The size distribution of the deposits was evaluated using *ImageJ* (Abramoff *et al.*, 2004; Schneider *et al.*, 2012).

We observe a high degree of focusing by the nozzle (central streak in Fig. 4). The droplet density is the highest straight behind the centre of the exit nozzle and decreases away from the spray centre. The central streak is approximately 250 µm wide. We note that, in the centre of the aerosol beam, the density is very high and the droplets overlap on the EM grid despite the rapid motion of the grid during droplet deposition. However, we observe that the individual droplets appear to be of approximately the same size as those deposited away from the centreline. At positions −3, −2, −1, 1, 2, 3 in Fig. 4, we see single round sucrose deposits, and the measured size distribution does not change over the entire grid. EM images in a somewhat different geometry show no central track and give the same size distributions as obtained here, indicating that our measurements are representative of the droplet sizes.

Fig. 6 and Table 1 show the measured distributions in size for the spots observed on the EM grid in Fig. 4. Measurements were performed at four different flow rates as indicated in the figure. This analysis was done on non-overlapping droplets, deposited off-centre from the nozzle opening. The results show that the liquid flow rate is a decisive parameter to tune the size of the droplets. At the highest investigated flow rate [400 nl min^{-1}; Fig. 6(*a*)], sucrose deposits with a median diameter of 520 nm were observed, corresponding to ∼1520 nm initial median droplet size. By reducing the flow rate to 350 and 300 nl min^{-1}, the median diameter of the deposits was decreased to 430 and 330 nm [Fig. 6(*b*) and 6(*c*)], and at 200 nl min^{-1} it was reduced to 70 nm [Figs. 6(*d*) and 5]. The histograms also show a significant number of sucrose deposits with diameters smaller than 200 nm under all investigated conditions. The calculated initial droplet diameters (lower scale in Fig. 6) were estimated for 50% sucrose droplets impacting on the grid.

Table 1
Median diameter of sucrose deposits measured on the electron microscopy grids and the corresponding diameter of the initial droplets formed at the GDVN.

Flow rate (nl min^{-1})	200	300	350	400
Measured median diameter of dry sucrose deposits on the EM grid (nm)	70	330	430	520
Calculated median volume of sucrose deposits (nm^3)	9.0×10^4	9.4×10^6	2.1×10^7	3.6×10^7
Calculated median sucrose volume of the deposits (nm^3)	4.5×10^4	4.7×10^6	1.0×10^7	1.8×10^7
Calculated median diameter of wet droplets leaving the GDVN [from equation (4)]	210	970	1260	1520
Diameter at peak counts in nm	∼120	∼360 ∼1000	∼440 ∼1320	∼1280

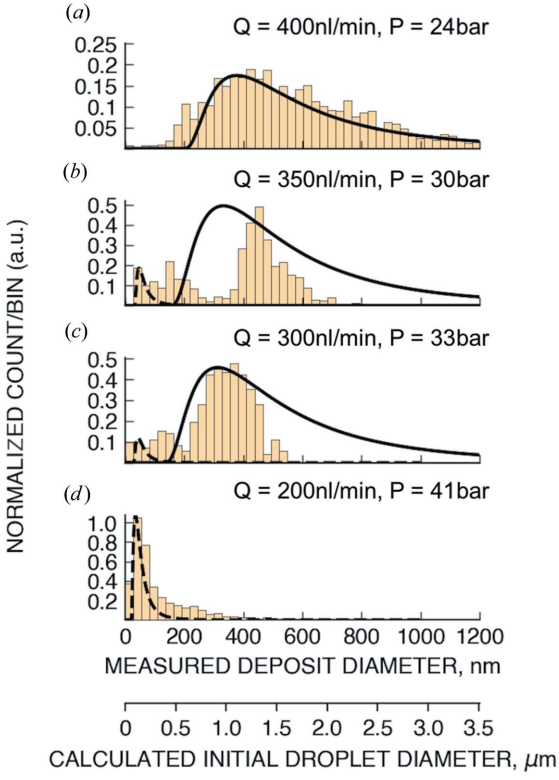

Figure 6
Histogram of measured deposit diameters on the EM grid as a function of flow rate. The second scale shows the estimated diameter of the droplets leaving the GDVN. The results show a clear trend of decreasing droplet size with decreasing flow rate. The solid lines are the lognormal probability density functions (arbitrary units) with mean $\ln(d_g)$ and standard deviation ln (GSD), where d_g is given by equation (5) with C_1 = 2.4 for our particular nebulizer geometry and C_2 = 18. The dashed lines are the lognormal probability density function (arbitrary units) with mean $\ln(d_g)$ and standard deviation ln (GSD), where d_g is given by equation (7) with k_0 = 3.5.

An additional line of evidence in support of this approach is provided by AFM measurements on the dried sucrose residues. The EM grids with sucrose deposits were transferred into an AFM and the volumes of numerous deposits were measured. In the AFM images we observe round spots that resemble shallow domes. Fig. 7 shows the AFM data;

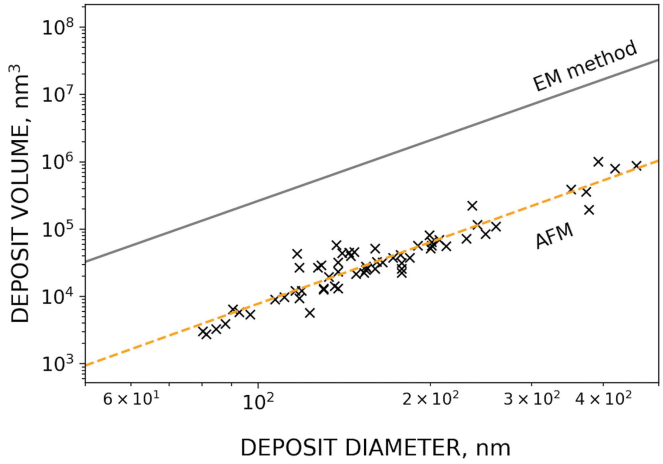

Figure 7
Comparison of measured volumes using the AFM and the EM method derived in Section 3.2. The dashed orange line is the fit function $0.0158d^{3.044}$ for the AFM data and the solid black line shows the volumes calculated using the EM method. The volume ratio between the two lines is about 30, leading to a particle diameter three times greater using our model than the directly measured deposits with the AFM.

measuring about 50 of these spots in the 80–500 µm range, we note that their volume increases with the cube of the footprint diameter.

This confirms that partially hydrated droplets impact onto the grid, sticky enough to cling to the surface owing to their high viscosity and surface tension. If the droplets had been fully dehydrated and bounced off after hitting the surface we would not expect to find remains on the surface; instead one might possibly expect indentations. Even if fully dehydrated sucrose balls were to leave any remains, the volume dependence of the footprint diameter would be less systematic, and possibly somewhat random rather than depending on the third power, like the relationship between diameter and volume.

The volumes of the deposits measured using the AFM differ from the volumes expected from the evaporation model. The deposits measured using the AFM are flatter than those estimated from the EM method (Fig. 7).

We see several possible reasons for this. For one, the deposits on the EM grids were previously imaged at high vacuum (10^{-6} mbar) and thus transitioned from partially hydrated to fully dehydrated. We have shown that the droplets dehydrate top down, leaving a deposit with the same diameter as the initial impacted droplet, but half the volume. Another reason for this deviation arises from the simplification that all droplets have a hemispherical shape at impact. Droplets were, however, accelerated in the passage through the funnel nozzle before impacting and getting squashed onto the substrate grid, eventually leading to flattened domes and correspondingly oversized footprints.

3.3. A theoretical description of the different flow regimes

At 400 nl min^{-1} liquid flow and 24 bar helium sheath-gas pressure, the GDVN exhibits a continuous smooth nebulization produced by a stable and clearly observable microjet [Fig. 2(*b*III)]. The jet emerges from a conical region and a thin liquid jet leaves this region. The jet is surrounded by and interacts with an expanding and turbulent helium stream, and it breaks up to produce droplets at small length scales, compatible with the Kolmogorov–Hinze theory (Shinnar, 1961; Lemenand *et al.*, 2003). We call this type of operation mode the 'conical' regime. We attribute this behaviour to that shown by pneumatic nebulizers of the 'flow focusing' (Gañán-Calvo, 1998) and 'flow blurring' (Gañán-Calvo, 2005; Rosell-Llompart & Gañán-Calvo, 2008) type, where smooth nebulization occurs above a threshold minimum flow rate. With our EM method, we observed a geometrical standard deviation (GSD) value of around 2.2. For this regime, we used a model proposed by Gañán-Calvo (2005) to predict the resulting droplet size distribution from a continuous turbulent mixing of the liquid and gas phase at the exit of a nozzle with exit diameter D. According to that model, the resulting droplet median diameter d_g is given by

$$d_g = C_1 D^{0.4} d_0^{0.6} (1 + C_2 \mathrm{Oh})(1 + 1/\mathrm{GLR})^{1.2}, \qquad (5)$$

where $d_0 = \gamma \Delta P^{-1}$ is the smallest length scale that can be produced from a given available mechanical energy per unit volume ΔP when invested against surface tension. C_1 is a fitting prefactor that would depend on the nozzle geometry, and C_2 is the fitting constant for viscous effects. GLR is the gas-to-liquid mass flow ratio (very large in our experiments), and $\mathrm{Oh} = \mu(\gamma\rho\, D)^{-1/2}$ is the Ohnesorge number. μ, ρ and γ are the liquid viscosity, density and surface tension, respectively. Thus, assuming GSD = 2.2, a lognormal distribution with mean $\ln(d_g)$ and standard deviation $\ln(\mathrm{GSD})$ provides a good prediction for the droplet size distribution, with $C_1 = 2.4$, as shown in Fig. 6(*a*).

When the flow rate is reduced to 350 or 300 nl min^{-1} liquid flow and 30 and 33 bar of helium feed pressure, the droplet size distribution departs significantly from the previous structure, exhibiting bimodal distributions as shown in Figs. 6(*b*) and 6(*c*). As we will see, this behaviour indicates a mixed operational mode and a transition between two regimes: The system would fluctuate between at least two configurations, yielding the observed structure of the droplet size spectrum. This bimodal spectrum is also compatible with the emission of more than one jet simultaneously, as has been observed independently (DePonte, 2019).

The most intriguing and valuable results for our purposes appear when the liquid flow rate is further reduced to 200 nl min^{-1} and the gas pressure increased to 41 bar. In this novel regime, the droplet size distribution falls well below any possible prediction from the Kolmogorov–Hinze theory if that is based on any macroscopic scale provided by the geometry of the nebulizer. Thus, one should rely on fluidic structures produced by the interaction of the liquid and gas streams alone, driven by a common available energy per unit volume ΔP. The narrow size distribution with a single mode indicates a very small capillary jet drawn by the gas stream (Gañán-Calvo, 1998), probably from the edges of the liquid feeding capillary, but other structures could also be imagined. Jets are no longer visible by optical microscopy at flow rates below ∼350 nl min^{-1}. The nebulizer geometry should favour the generation of the smallest stable capillary jet possible, even using an asymmetric arrangement as suggested by Acero *et al.* (2013). In our case, an asymmetrically shaped capillary tip with an advanced region resembling that of a partially bevelled needle is used [see Fig. 2(*b*)].

In Fig. 6, we fit a lognormal probability density function with a mean $\ln(d_g)$ to the size distribution deduced from the EM method, where d_g is given by equation (7) below. This fit is based on a dominant autonomous flow scale d entirely due to the turbulent breakup of the capillary stream generated (Rosell-Llompart & Gañán-Calvo, 2008). This scale d is obtained using the same Kolmogorov–Hinze theoretical arguments, but assuming that the large scale of the turbulent cascade in the motion of the liquid is provided by the size of the initial jet formed at the tip of the feeding liquid capillary [see Fig. 2(*b*)], leading to (Rosell-Llompart & Gañán-Calvo, 2008)

$$d/d_0 \simeq (Q/Q_0)^{1/5}. \qquad (6)$$

Here, $Q_0 \simeq (\gamma^4 \rho^{-1} P^{-3})^{1/2}$ is the characteristic minimum flow rate to have a stable continuous liquid stream held by capillary

forces, for a liquid with density ρ subject to a pressure difference ΔP. If the ultimate scale d is identified as the most probable droplet size d_g for this very small liquid flow rate, one would have

$$d_g = k_0(Q/Q_0)^{1/5}d_0, \quad (7)$$

where k_0 is a fitting prefactor of order unity. Making $k_0 = 3.5$ and assuming a lognormal droplet size distribution like in the case of a 'conical' liquid flow, with the same GSD but a median given by equation (7), one obtains the general agreement shown in Fig. 6(*d*).

This result demonstrates that predictable droplet sizes comparable to those obtained by electrospray ionization can be produced by purely mechanical means by GDVNs, without altering the ionic composition or electrochemical equilibrium of the liquid solution. Comparable droplet sizes formed by electrospray ionization would need an equivalent pressure drop of about 140 bar (Gañán-Calvo & Montanero, 2009). The pressure drops used here were 41, 33, 30 and 24 bar at 200, 300, 350 and 400 nl min^{-1} liquid flow rates, respectively, creating conditions not far from the case of electrospray ionization. The mechanical breakup and mixing of jets and droplets in the helium gas stream at the exit of the GDVN is expected to have an additional influence on the final droplet size distributions measured here. The droplet formation is unstable at 300 and 350 nl min^{-1}, where we observe a bimodal size distribution of the sucrose deposits and the fits break down as shown in Figs. 6(*b*) and 6(*c*) and Table 1.

4. Conclusion and outlook

In summary, our EM method allows us to study the size distribution in high-density polydisperse aerosols formed by GDVNs and other aerosolizing devices. The results show that a GDVN can be tuned to generate droplets with submicrometre size distributions, depending on the liquid flow rate, and demonstrate the role of operating and geometrical parameters and their influence on the consistent formation of submicrometre droplets. This method allows evaluation of the design and operation of GDVNs or other aerosolizing devices and tailoring of their performance for numerous highly valued purposes.

Funding information

This work was supported by the Swedish Research Council, the Knut and Alice Wallenberg Foundation, the European Research Council, the Röntgen–Ångström Cluster, and the projects Advanced research using high intensity laser produced photons and particles (CZ.02.1.01/0.0/0.0/16_019/0000789) and Structural dynamics of biomolecular systems (CZ.02.1.01/0.0/0.0/15_003/0000447) from the European Regional Development Fund. JA acknowledges support of the Ministry of Education, Youth and Sports as part of targeted support from the National Programme of Sustainability II and the Chalmers Area of Advance in Material Science. AMGC is grateful for support from the Ministerio de Economía, Industria y Competitividad, Plan Estatal 2013–2016 Retos, project No. DPI2016-78887-C3-1-R.

References

Abramoff, M. D., Magalhaes, P. J. & Ram, S. J. (2004). *Biophoton. Int.* **11**, 36–42.
Acero, A. J., Rebollo-Muñoz, N., Montanero, J. M., Gañán-Calvo, A. M. & Vega, E. J. (2013). *J. Micromech. Microeng.* **23**, 065009.
Awel, S., Kirian, R. A., Wiedorn, M. O., Beyerlein, K. R., Roth, N., Horke, D. A., Oberthür, D., Knoska, J., Mariani, V., Morgan, A., Adriano, L., Tolstikova, A., Xavier, P. L., Yefanov, O., Aquila, A., Barty, A., Roy-Chowdhury, S., Hunter, M. S., James, D., Robinson, J. S., Weierstall, U., Rode, A. V., Bajt, S., Küpper, J. & Chapman, H. N. (2018). *J. Appl. Cryst.* **51**, 133–139.
Daurer, B. J., Okamoto, K., Bielecki, J., Maia, F. R. N. C., Mühlig, K., Seibert, M. M., Hantke, M. F., Nettelblad, C., Benner, W. H., Svenda, M., Tîmneanu, N., Ekeberg, T., Loh, N. D., Pietrini, A., Zani, A., Rath, A. D., Westphal, D., Kirian, R. A., Awel, S., Wiedorn, M. O., van der Schot, G., Carlsson, G. H., Hasse, D., Sellberg, J. A., Barty, A., Andreasson, J., Boutet, S., Williams, G., Koglin, J., Andersson, I., Hajdu, J. & Larsson, D. S. D. (2017). *IUCrJ*, **4**, 251–262.
DePonte, D. P. (2019). Personal communication.
DePonte, D. P., Weierstall, U., Schmidt, K., Warner, J., Starodub, D., Spence, J. C. H. & Doak, R. B. (2008). *J. Phys. D Appl. Phys.* **41**, 195505.
Ekeberg, T., Svenda, M., Abergel, C., Maia, F., Seltzer, V., Claverie, J. M., Hantke, M., Jonsson, O., Nettelblad, C., van der Schot, G., Liang, M., DePonte, D. P., Barty, A., Seibert, M. M., Iwan, B., Andersson, I., Loh, N. D., Martin, A. V., Chapman, H., Bostedt, C., Bozek, J. D., Ferguson, K. R., Krzywinski, J., Epp, S. W., Rolles, D., Rudenko, A., Hartmann, R., Kimmel, N. & Hajdu, J. (2015). *Phys. Rev. Lett.* **114**, 098102.
Gañán-Calvo, A. M. (1998). *Phys. Rev. Lett.* **80**, 285–288.
Gañán-Calvo, A. M. (2005). *Appl. Phys. Lett.* **86**, 214101.
Gañán-Calvo, A. M., DePonte, D. P., Herrada, M. A., Spence, J. C. H., Weierstall, U. & Doak, R. B. (2010). *Small*, **6**, 822–824.
Gañán-Calvo, A. M. & Montanero, J. M. (2009). *Phys. Rev. E*, **79**, 066305.
Hantke, M. F., Hasse, D., Maia, F., Ekeberg, T., John, K., Svenda, M., Loh, N. D., Martin, A. V., Timneanu, N., Larsson, D. S. D., van der Schot, G., Carlsson, G. H., Ingelman, M., Andreasson, J., Westphal, D., Liang, M. N., Stellato, F., DePonte, D. P., Hartmann, R., Kimmel, N., Kirian, R. A., Seibert, M. M., Muhlig, K., Schorb, S., Ferguson, K., Bostedt, C., Carron, S., Bozek, J. D., Rolles, D., Rudenko, A., Epp, S., Chapman, H. N., Barty, A., Hajdu, J. & Andersson, I. (2014). *Nat. Photon.* **8**, 943–949.
Holyst, R., Litniewski, M., Jakubczyk, D., Kolwas, K., Kolwas, M., Kowalski, K., Migacz, S., Palesa, S. & Zientara, M. (2013). *Rep. Prog. Phys.* **76**, 034601.
Lemenand, T., Della Valle, D., Zellouf, Y. & Peerhossaini, H. (2003). *Int. J. Multiphase Flow*, **29**, 813–840.
Patel, A. R. & Vavia, P. R. (2007). *Indian J. Exp. Biol.* **45**, 166–174.
Rosell-Llompart, J. & Gañán-Calvo, A. M. (2008). *Phys. Rev. E*, **77**, 036321.
Schneider, C. A., Rasband, W. S. & Eliceiri, K. W. (2012). *Nat. Methods*, **9**, 671–675.
Schot, G. van der, Svenda, M., Maia, F., Hantke, M., DePonte, D. P., Seibert, M. M., Aquila, A., Schulz, J., Kirian, R., Liang, M., Stellato, F., Iwan, B., Andreasson, J., Timneanu, N., Westphal, D., Almeida, N. F., Odic, D., Hasse, D., Carlsson, G. H., Larsson, D. S. D., Barty, A., Martin, A. V., Schorb, S., Bostedt, C., Bozek, J. D., Rolles, D., Rudenko, A., Epp, S., Foucar, L., Rudek, B., Hartmann, R., Kimmel, N., Holl, P., Englert, L., Loh, N. T. D., Chapman, H. N.,

Andersson, I., Hajdu, J. & Ekeberg, T. (2015). *Nat. Commun.* **6**, 5704.
Seibert, M. M., Ekeberg, T., Maia, F., Svenda, M., Andreasson, J., Jönsson, O., Odić, D., Iwan, B., Rocker, A., Westphal, D., Hantke, M., DePonte, D. P., Barty, A., Schulz, J., Gumprecht, L., Coppola, N., Aquila, A., Liang, M. N., White, T. A., Martin, A., Caleman, C., Stern, S., Abergel, C., Seltzer, V., Claverie, J. M., Bostedt, C., Bozek, J. D., Boutet, S., Miahnahri, A. A., Messerschmidt, M., Krzywinski, J., Williams, G., Hodgson, K. O., Bogan, M. J., Hampton, C. Y., Sierra, R. G., Starodub, D., Andersson, I., Bajt, S., Barthelmess, M., Spence, J. C. H., Fromme, P., Weierstall, U., Kirian, R., Hunter, M., Doak, R. B., Marchesini, S., Hau-Riege, S. P., Frank, M., Shoeman, R. L., Lomb, L., Epp, S. W., Hartmann, R., Rolles, D., Rudenko, A., Schmidt, C., Foucar, L., Kimmel, N., Holl, P., Rudek, B., Erk, B., Hömke, A., Reich, C., Pietschner, D., Weidenspointner, G., Strüder, L., Hauser, G., Gorke, H., Ullrich, J., Schlichting, I., Herrmann, S., Schaller, G., Schopper, F., Soltau, H., Kühnel, K. U., Andritschke, R., Schröter, C. D., Krasniqi, F., Bott, M., Schorb, S., Rupp, D., Adolph, M., Gorkhover, T., Hirsemann, H., Potdevin, G., Graafsma, H., Nilsson, B., Chapman, H. N. & Hajdu, J. (2011). *Nature*, **470**, 78–81.
Shang, L. R., Cheng, Y. & Zhao, Y. J. (2017). *Chem. Rev.* **117**, 7964–8040.
Shinnar, R. (1961). *J. Fluid Mech.* **10**, 259–275.
Uetrecht, C., Rose, R. J., van Duijn, E., Lorenzen, K. & Heck, A. J. R. (2010). *Chem. Soc. Rev.* **39**, 1633–1655.
Wu, J., Kong, T. T., Yeung, K. W. K., Shum, H. C., Cheung, K. M. C., Wang, L. Q. & To, M. K. T. (2013). *Acta Biomater.* **9**, 7410–7419.